Environmental Science
Water Research & Technology

Solar-driven evaporators for water treatment: challenges and opportunities

Journal:	*Environmental Science: Water Research & Technology*
Manuscript ID	EW-CRV-08-2020-000725
Article Type:	Critical Review

Water Impact Statement

Solar-driven evaporators provide a sustainable way to obtain freshwater from saltwater and wastewater; design strategies for efficient, durable, and integratable evaporators are crucial for the implementation of this technique.

ARTICLE

Solar-driven evaporators for water treatment: challenges and opportunities

Received 00th January 20xx,
Accepted 00th January 20xx

DOI: 10.1039/x0xx00000x

Shao-Lin Wu,[a] Honglei Chen,[a] Hua-Li Wang,[a] Xiaolan Chen,[a] Hao-Cheng Yang,*[a,b] and Seth B. Darling*[c,d]

Solar-driven evaporation is an emerging process to acquire freshwater from saline water or wastewater, in which photothermal materials play a crucial role. Significant effort has been devoted to promoting energy conversion efficiency by material and device design. In the current review, we discuss the major factors affecting evaporator efficiency and long-term performance, including selection of photothermal materials, promotion of evaporation efficiency, and solutions to the problem of scaling. Both the material components and structure will affect the absorption and reflection of the incident light, and the evaporation efficiency can be enhanced by reducing heat loss, enlarging surface area, and recycling latent heat. Scaling can be addressed by tailoring surface properties and structure.

1. Introduction

Water security is one of the primary global sustainable development goals. Climate change as well as fast urbanization and population growth have aggravated water stress, and each will worsen in the coming decades.[1,2] While infrastructure and policy strategies will be essential to meeting this challenge, increasing supplies of fit-for-purpose water is also a critical goal. In many cases, expanding supply will require turning to more challenging source waters, such as seawater or wastewater. Technologies exist to convert these sources into fit-for-purpose streams, but often at a high energy and economic cost. There is a pressing need, therefore, for new strategies to improve energy efficiency or to increase utilization of low-cost, renewable energy sources for water treatment.

Seawater is essentially an inexhaustible source. However, producing fresh water through desalination by distillation[3] or reverse osmosis (RO) plants[4] consumes significant energy, which inextricably couples clean water acquisition to energy as part of the energy-water nexus. Thermodynamics imposes energy constraints on separating water from salt ions, but if the energy for these processes can be drawn from low-carbon and plentiful sources, the burden on the overall energy system can be lessened. Sunlight is, by far, the most abundant such energy source. Electricity from photovoltaic systems, for example, can be exploited for powering pumps in a RO desalination plant.[5,6] Alternatively, solar energy can also be used to drive water distillation. Even though a phase-change process such as distillation will require more energy than RO, the systems can be far simpler to implement and may therefore be suitable for smaller scale applications or in those locations where there is less infrastructure in place. The case for such solar-driven evaporators is perhaps even stronger with wastewater treatment, where fouling can present a tremendous challenge for membrane filtration.[7]

Since water itself is a poor absorber of sunlight, one must introduce photothermal materials that can harvest a broad spectrum of light and convert that energy to heat. Photothermal materials have found wide use in the biomedicine field, such as with photothermal therapy, but it was only within the past few years that these materials have been implemented in solar-driven evaporation. Plasmonic nanoparticles were dispersed in the bulk solution for solar heating and evaporation in some early research.[8,9] However, most of the generated heat is wasted in elevating the bulk temperature, so that the evaporation efficiency is relatively low. Rather than heating the entire body of water to be treated, energy losses can be minimized by localizing the heat at the evaporation (air/water) interface. This localization can be enabled through the use of photothermal materials that are floated on top of the water.[10–15] The overall evaporation efficiency can be calculated by detecting the mass change under constant light irradiation. The instantaneous efficiency is calculated as $\eta=\dot{m}h/P$, in which $\dot{m}$ is the difference between the evaporation rates in light and dark environments, h is the specific enthalpy change of liquid water to vapor, and P is the light power.[16] The evaporation efficiency is mainly restricted

[a] School of Chemical Engineering and Technology, Sun Yat-Sen University, Zhuhai, 519082, China, E-mail: yanghch8@mail.sysu.edu.cn
[b] Southern Marine Science and Engineering Guangdong Laboratory (Zhuhai), Zhuhai, 519082, China
[c] Center for Molecular Engineering and Chemical Sciences and Engineering Division, Argonne National Laboratory, Lemont, IL 60439, USA, E-mail: darling@anl.gov
[d] Advanced Materials for Energy-Water Systems (AMEWS) Energy Frontier Research Center, Argonne National Laboratory, Lemont, IL 60439, USA
† Footnotes relating to the title and/or authors should appear here.
Electronic Supplementary Information (ESI) available: [details of any supplementary information available should be included here]. See DOI: 10.1039/x0xx00000x

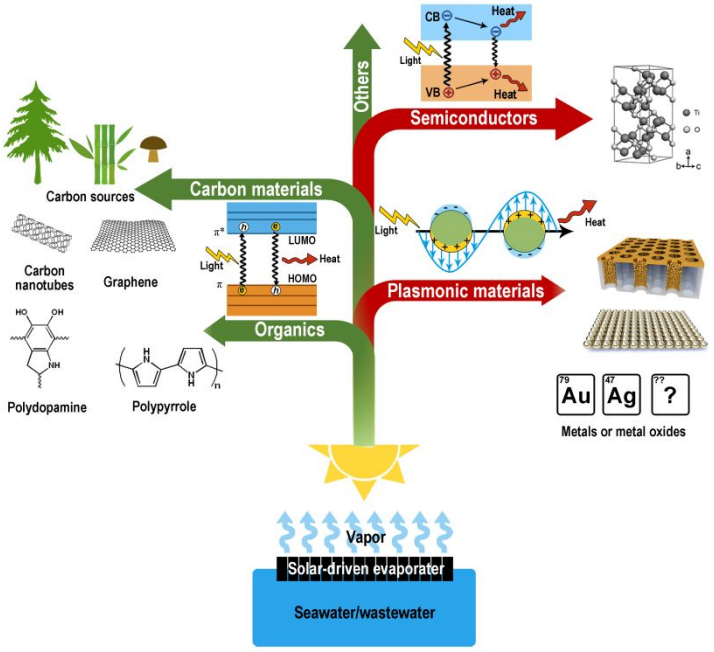

Fig. 1 Typical photothermal materials and their light-to-heat conversion mechanisms.[23,27,40,43,46,69,78,81]

by two factors: the light-to-heat conversion, affected by the reflectance, absorption spectrum, and other energy conversion processes, and the water-to-vapor conversion, influenced by the heat loss (i.e., conduction, convection, and radiation).

There are several published reviews on material and architecture design of solar-driven evaporators;[12,13,15,17–19] here, we focus on the major issues for promoting evaporation efficiency as well as long-term stability of the evaporator. In particular, we elaborate on emerging strategies and their mechanisms to alleviate scaling during desalination, which is only briefly discussed in existing reviews. Firstly, we summarize the reported photothermal materials including carbon, metal nanoparticles and their compounds, semiconductors, polymers and other hybrid materials, as well as their light-to-heat conversion mechanisms. The light absorption and subsequent light-to-heat conversion efficiency are major factors affecting the overall evaporation performance. We present how to promote heat utilization for evaporation through heat management by structure design, which is another key factor in evaporation efficiency. Lastly, we discuss arguably the biggest challenge hindering commercial application of solar-driven evaporators, scaling, and several promising solutions. Although scaling generally occurs after a period of evaporation and has negligible effect on the initial efficiency, it will compromise the long-term performance and overall efficiency.

2. How to select a photothermal material

The overall efficiency of a solar-driven evaporator includes two parts: the photothermal efficiency, referring to how much energy is transformed from light to heat, and the thermal evaporation efficiency, referring to how much transformed heat is used in evaporation. It should be mentioned that the evaporation efficiency in many studies refers to the proportion of light used in evaporation, which is the product of the two parts. Photothermal efficiency is determined by the intrinsic properties and architecture of photothermal materials. An ideal photothermal material requires wide light absorption, low reflection/transmission, and the absence of parasitic energy conversions such as fluorescence radiation and photoelectric conversion.

Carbon materials are common in solar steam generation owing to their wide absorption spectra, low cost, and high accessibility. The light-to-heat conversion mechanism of carbon materials, as well as some organic materials, is the lattice vibrations.[12,17] The electrons can be easily excited from the π orbital to π* orbital with a small energy input. Increased π bonds narrow the energy gap between the highest occupied molecular orbital (HOMO) and the lowest unoccupied molecular orbital (LOMO). The light is absorbed to promote an electron from the ground state to a higher energy orbital when it matches possible electronic transition within the molecule, and the heat is released during the inverse process. One of the earliest studies in this field demonstrated an evaporator composed of an exfoliated graphite layer on a hydrophilic carbon foam.[20] In another research, the authors directly dip-coated carbon black (CB) with polydimethylsiloxane (PDMS) on gauze to fabricate a superhydrophobic floating evaporator.[21] Numerous research groups have developed solar-driven evaporators based on carbon nanomaterials including carbon nanotubes (CNTs),[22–25] graphene,[26–33] and carbon dots.[34] Evaporators can be fabricated directly from these nanomaterials or by compositing them on a substrate or template. In general, conventional evaporators require interconnected porous structure to provide water channels from the bulk to the surface. One of the most widely applied strategies to fabricate a porous graphene structure is

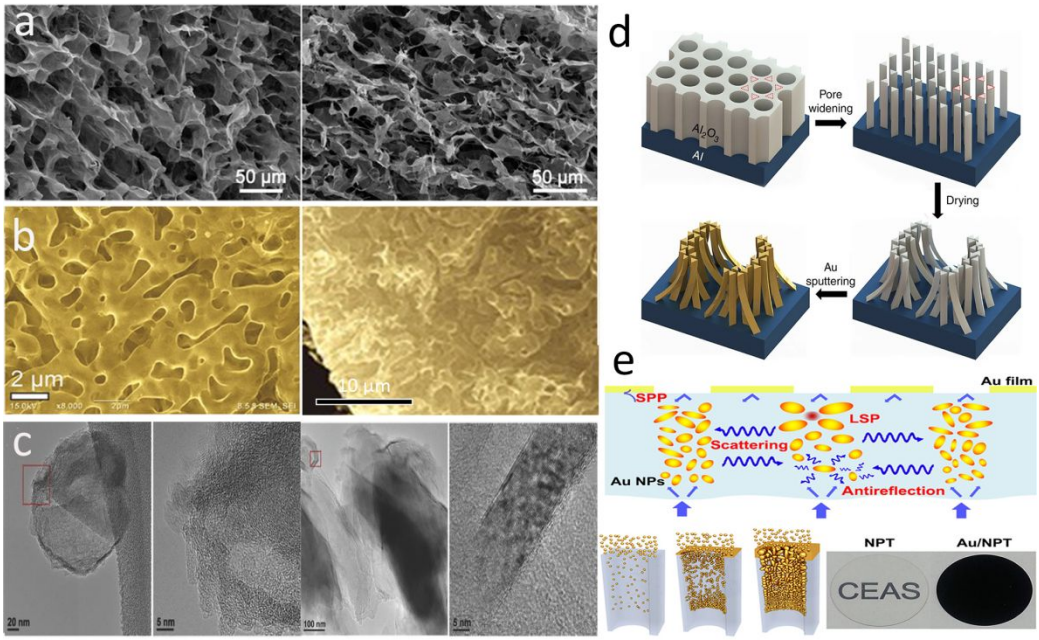

Fig. 2 Structures of photothermal materials. a) Porous graphene produced by freeze-drying;[27] b) N-doped graphene grown on a porous Ni substrate;[31] c) carbon nanoparticles and nanoplatelets with amorphous and graphite-like structures in Chinese ink;[36] d) gold nanopillars based on an AAO template;[47] e) Random deposition of gold nanoparticles on AAO channels.[46]

freeze-drying, in which the pores are templated by the ice crystals.[26,27,33] For example, Hu *et al.* directly freeze-dried a mixture of graphene oxide (GO), multi-wall CNTs, and sodium alginate to fabricate an aerogel for solar steam generation.[27] A porous graphene-based structure can be also achieved by growing graphene on a 3D skeleton (Fig. 2a). For example, Ito *et al.* grew graphene and N-doped graphene on nanoporous Ni substrates through chemical vapor deposition (CVD) and obtained a 3D graphene structure after removing the catalytic Ni template (Fig. 2b).[31] Ren *et al.* fabricated a hierarchical photothermal sponge by vertically growing graphene nanoplates on a 3D foam skeleton through plasma-enhanced CVD.[30] Carbon nanomaterials can be also composited onto a substrate through vacuum filtration of their suspension.[22,29,35] Composited with a thermo-insulating substrate, the obtained photothermal films can localize the heating at the interface. Carbon nanomaterials have also been blended within a hydrogel. For example, Singht *et al*. embedded carbon dots in a carboxymethyl cellulose/chitosan network to fabricate a hydrogel evaporator.[34] Our group developed a membrane evaporator based on Chinese ink, an ancient carbon nanomaterial.[36] The Chinese ink is made of soot, animal glue, and other additives, which can be uniformly coated and strongly adhered on the substrate materials. Compared with other synthetic carbon materials, the carbon in Chinese ink includes both carbon nanoparticles and nanoplatelets with amorphous and graphite-like structures, exhibiting broad light absorption (Fig. 2c). Atomic layer deposition was conducted to integrate the ink coating with a polymer membrane substrate against re-dispersion.

Another important source of photothermal carbon materials is carbonized organic materials, both natural and synthetic. For example, Hu's group developed a series of wood-based evaporators by carbonizing the top surface of wood.[37–39] Straight pores extending hundreds of micrometers through the material can help to manage scale formation, which is discussed in a later section. A carbonized mushroom evaporator was developed by Zhu's group, in which the stipe served as a 1D water channel, and the pileus provided larger evaporation area.[40] Other natural materials like sucrose,[41] sunflower,[42] bamboo,[43] and lotus seedpods[44] were also used as the carbon sources for photothermal materials. Beyond natural materials, synthetic materials have also been explored. For example, Zhu *et al.* fabricated a highly porous N-doped carbon sponge by carbonizing low-cost melamine.[45]

Metallic nanomaterials, such as gold,[46–48] silver,[49] palladium,[50] aluminium,[51] copper,[52,53] nickel,[54,55] and indium[56] nanoparticles, represent another category of photothermal material, in this case based on plasmonic absorption. When metallic nanomaterials absorb incident light that matches the natural frequency of the metallic electrons, the free electrons collectively oscillate near the metal-dielectric interface, known as surface plasmons.[11,12] Surface plasmons include three modes for effective light-to-heat conversion: surface plasmon polaritons (SPP) in which the plasmons can propagate along with the metal-dielectric interface, localized surface plasmon resonance (LSPR) in which the plasmons are located in specific positions, and hybridized plasmonic modes.[57] Attributed to the intense light-to-heat capacity based on the LSPR effect, gold nanoparticles have attracted tremendous interest in solar steam generation. Deng's group fabricated gold nanoparticle films via self-assembly process induced by acid vapor diffusion to confine the plasmonic heat at the air-water interface.[58] However, the substrate-free film of gold nanoparticles is fragile therefore struggles to offer reusability in practical applications. To address this issue, the same group utilized an air-laid paper to support

the gold nanoparticle film for enhanced mechanical stability and heat insulation.[59] Some inorganics are not intrinsically plasmonic materials but exhibit plasmon-like properties, for example, tellurium,[60] and some high-index all-dielectric inorganics such as germanium[61] and silicon[62] can also enable light-to-heat conversion by Mie-type resonances.

Similar to carbon materials, plasmonic nanoparticles are commonly integrated with a substrate or template for high-performance evaporation devices. In some cases, the substrate or template provides extra opportunities to adjust the structure of plasmonic absorbers for promoted photothermal efficiency by covering the whole solar spectrum. For example, Bae *et al.* fabricated a self-aggregated nanowire bundle array based on anodic aluminium oxide (AAO) and then sputtered gold on it to construct an adiabatic nanofocusing structure of surface plasmons (Fig. 2d).[47] In this designed structure, the merged nanowire bundles with a small taper angle and discrepant nanogaps absorbed shorter wavelength light in the ultraviolet, visible, and near-infrared region, and the funnel shapes in the cross-section enabled mid-infrared absorption. Such structure achieved nearly 91% absorption across the wavelengths from 400 to 2500 nm. Zhu's group assembled gold nanoparticles into an AAO template with tunable pore size by physical vapor deposition.[46] Attributed to the precise adjustment of AAO pore size and deposition process, gold nanoparticles with widely distributed sizes were decorated on the walls of those channels (Fig. 2e). The random distribution of gold nanoparticles caused a strong hybridized LSPR effect while the straight pores reduced the light reflectance, resulting in wide absorption from 400 to 10000 nm. Alternatively, the gold nanoparticles could be replaced by much cheaper aluminium particles.[51] The bandwidth and cutoff wavelength of a plasmonic absorber could also be adjusted by the template pore size for a selective spectrum.[48]

Semiconductor-based photothermal materials such as metal oxides and chalcogenides have been also widely used in solar evaporators over the past few years. There are two different light-to-heat conversion mechanisms of semiconductor-based absorbers. One is the LSPR effect explained above, such as with CuS,[63] Cu_7S_4,[64] and non-stoichiometric WO_x[65,66] nanomaterials. For example, Zhang *et al.* developed a facile and economical strategy to synthesize shape-controlled high-quality Cu_7S_4 nanocrystals, of which the organic phase was assembled into a dense film for interfacial solar steam generation.[64] Chang and co-workers decorated hydrophobic PDMS-coated $W_{18}O_{49}$ mesocrystals onto hydrophilic polytetrafluoroethylene membranes to fabricate a high-efficiency evaporator.[65] The other conversion mechanism is non-radiative relaxation induced by intrinsic bandgap absorption of semiconductors, such as with black titania,[67] TiO_x,[68] Ti_2O_3,[69] and Fe_3O_4[70] nanoparticles. For example, Wang *et al.* prepared nanosized Ti_2O_3 by ball milling for interfacial solar evaporation, which achieved nearly 100% internal and about 92% external light-to-heat conversion efficiency due to the narrow bandgap and nanoscale features.[69] MXenes are another kind of emerging photothermal material, which have a similar 2D structure to GO. These materials have potential for outstanding light-to-heat conversion in evaporation applications.[71–73] Metal nitrides such as TiN, although not strictly semiconductors, also offer outstanding photothermal effects based on the LSPR mechanism. TiN nanoparticles were composited with ceramic fiber wool and carbonized wood to fabricate an enhanced evaporator.[74,75] Traver and co-workers compared the photothermal performance of the Group Ⅳ metal nitride (TiN, ZrN, HfN) nanoparticles, in which the HfN performs the best.[76]

In some instances, performance can be improved by combining several materials to integrate complementary properties. The composite of several photothermal materials, such as carbon-semiconductor nanomaterials, is used to improve solar spectrum absorption. For instance, a composite film of single-walled CNTs and MoS_2 exhibited higher absorption (82%~95%) than pure single-walled CNT films (63%) across the wavelengths from 300 to 2500 nm.[25] The absorption capacity of the composite film could be further improved by increasing the thickness of MoS_2 nanosheets. In addition, Yi and co-workers blended commercial TiO_2 and aluminium powders to fabricate the black Al-Ti-O hybrid by planetary-milling, in which the aluminium component induced the LSPR effect, broadened the absorption spectrum to the infrared region, and partially reduced TiO_2 for enhanced absorption capacity.[77]

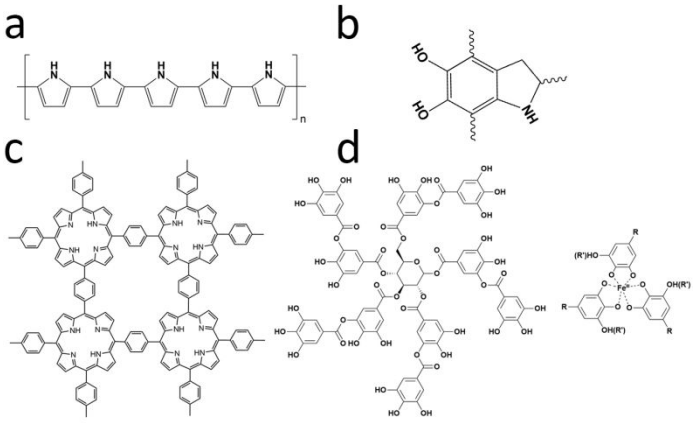

Fig. 3 Molecular structures of a) PPy, b) PDA, c) POF and d) tannic acid/ferric tannate.

Beyond inorganic photothermal materials, organic materials with a wide conjugated structure such as polypyrrole (PPy)[78–80] and polydopamine (PDA)[81] are also candidates for photothermal materials, mainly based on lattice vibrations that achieve light-to-heat conversion (Fig. 3a and b). For example, Wang's group deposited PPy coating onto stainless steel mesh to fabricate a self-healable photothermal membrane.[78] The durability of the

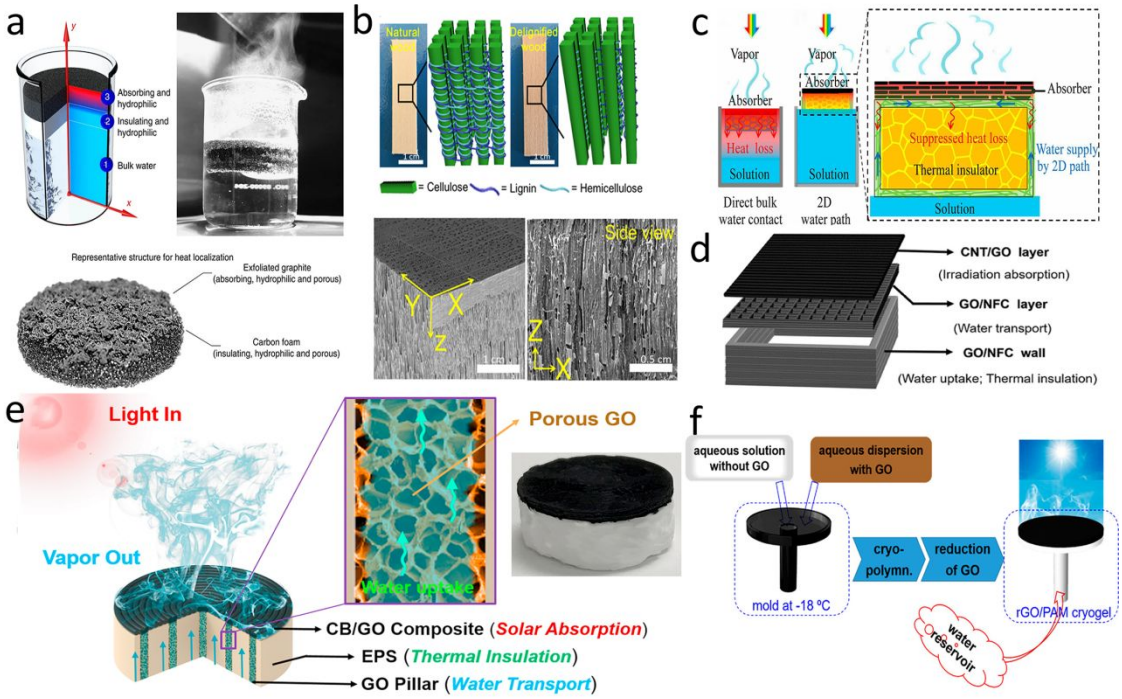

Fig. 4 Evaporators with a thermal barrier. a) Double-layer structure composed of exfoliated graphite deposited on carbon foam;[20] b) delignified wood with aligned channels;[88] c) confined 2D water path for reducing heat conduction loss;[29] d) concave structure of 3D printed all-in-one evaporator;[102] e) jellyfish-like evaporator with confined 1D water channels;[32] f) mushroom-like evaporator.[104]

PPy-coated membrane was improved by hydrophobicity restoration. Additionally, Yu and co-workers fabricated a hierarchically nanostructured gel comprised of polyvinyl alcohol and PPy.[80] The composite gel with internal gaps, micron-scale channels, and molecular meshes can fully utilize the input solar energy and achieved high evaporation efficiency. Recently, we developed a black porphyrin-based covalent organic framework, called porphyrin organic framework (POF), as a novel photothermal coating on various porous substrates, which displayed broad harvesting across the visible and near-infrared range (Fig. 3c).[82] Natural components, such as, ferric tannate[83–85] (Fig. 3d) and coffee colloids[86], can also serve as a green photothermal material for solar steam generation.

3. How to promote the evaporation efficiency

3.1 Integrating with a thermal barrier

Heat management is crucial for promoting thermal evaporation efficiency. Incident solar energy is absorbed by the photothermal layer and ultimately split into five energy output pathways: reflective solar radiation, water evaporation, radiative heat loss, convective and conduction heat loss to ambient air, and heat conduction loss to the bulk water.[18] Owing to the relatively high thermal conductivity of water, heat conduction loss to the bulk can be a troublesome issue that impairs evaporation efficiency. One of the most straightforward ways to reducing heat transfer is to build a heat-insulating layer between the absorber and underlying water. Ghasemi *et al.* first reported a double-layer structure with a top light absorber composed of exfoliated graphite and a bottom carbon foam as a thermal barrier to minimize the dissipated energy (Fig. 4a).[20] The evaporator exhibited an impressive thermal conversion efficiency (85%) under ten suns irradiation. Such a structure is widely adopted in evaporator design because the heat barrier can not only reduce the heat loss but also provide mechanical support.

After the first attempt, various thermal barriers were developed to ensure effective water transport through the evaporator.[22,87–95] To achieve hydrophilic channels, silica,[22] wood,[88,90,95] sugarcane stems,[94] and cellulose nanofibrils[87] were applied to replace carbon foam as a heat barrier. Beyond the composition of the thermal barrier, structure of the underlying supports can also influence heat transfer. For example, mesoporous wood exhibited anisotropic thermal conduction in that the absorbed heat preferred to transfer along (0.35 W m^{-1} K^{-1}) rather than across (0.11 W m^{-1} K^{-1}) the growth direction of the wood[90], confining the heat at the evaporation in-plane surface and suppressing heat conduction loss to the bulk water. Mesoporous wood exhibited superior heat-insulating property relative to the widely used polystyrene (PS) foam (~0.03 W m^{-1} K^{-1}). Moreover, the porosity of the heat barrier could be adjusted to optimize heat insulation. Chen *et al.* removed the hydrophobic lignin from the wood to introduce more defects and air space for improved water transport and less heat conduction loss to the bulk water (Fig. 4b).[88] Liu and co-workers demonstrated how the porosity affected the balance between mass transfer and heat transfer, proposing an optimal porosity of 0.52 for the double-layer evaporator.[91]

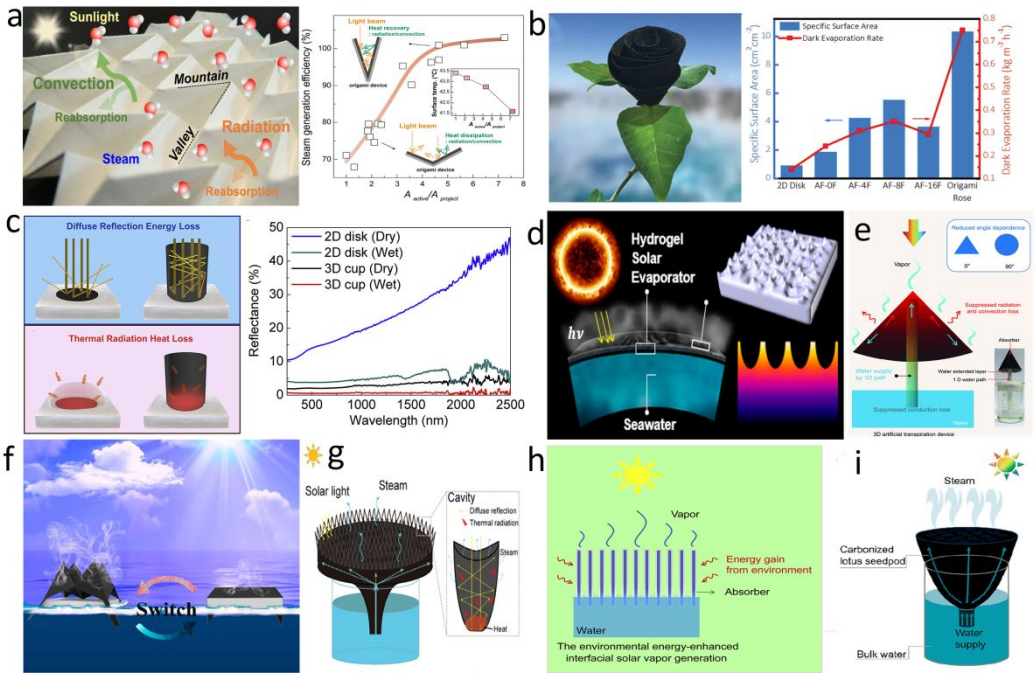

Fig. 5 Enlarging surface area for enhanced evaporation. a) Periodic mountain-like and valley-like folds for heat management and enhanced evaporation;[107] b) rose-like evaporator and comparison of evaporation rate with other origami-based evaporators;[108] c) light-reflectance and heat loss in a 2D disk evaporator and a 3D cup evaporator;[113] d) hydrogel-based evaporator with sharply dimpled structure;[111] e) hollow GO cone;[112] f) origami-based switchable 2D/3D evaporator;[109] g) carbonized sunflower head evaporator;[42] h) low-temperature evaporator for "cool evaporation";[114] i) carbonized lotus seedpod evaporator.[44]

A porous thermal barrier also suffers from inevitable heat transfer though the 3D water channel network. To address this problem, Zhu's group proposed a concept of confined 2D water path to minimize heat conduction loss (Fig. 4c).[29] A cellulose layer was wrapped over the surface of the PS foam, and the bottom of the cellulose layer was immersed into the water, enabling water transport to the top GO surface by the capillary effect. The heat was located at the evaporation interface so that the temperature of the bulk water remained nearly constant. Such configuration has been widely used in evaporator design.[96–102] For example, Luo *et al.* constructed a CB patterned evaporator by laser printing on the air-laid paper-wrapped expanded polyethylene foam structure. Both heat and mass transfer happened between the adjacent patterns, which alleviated the energy loss.[100] Hu's group utilized layer-by-layer 3D printing to fabricate an all-in-one evaporator with a concave structure, in which the GO/nanofibrillated cellulose wall provided the 2D water paths for water wicking (Fig. 4d).[102] The air inside the wall of the concave structure served as a desirable heat barrier against heat conduction loss.

The same group also developed an integrated jellyfish-like evaporator with a confined 1D water path by 3D printing, which consisted of a CB/GO disc as the photothermal absorber, vertical 3D-printed GO pillars as the 1D channel, and an expanded PS support as a heat barrier (Fig. 4e).[32] In addition, Liu *et al* fabricated a tree transpiration-inspired capillary-driven pump with a 1D water path to reduce heat loss.[103] Compared with the 2D water path, the 1D water path further reduces the contact area between the evaporator and the bulk water, effectively suppressing heat dissipation. Following this concept, He *et al.* adopted cryopolymerization to fabricate a mushroom-like evaporator composed of reduced GO/polyacrylamide (PAM) pileus and PAM cryogel stipe (Fig. 4f).[104] The porous and hydrophilic stipe acted as the 1D water path for water supply and heat management.

Recently, some indirect-contact and contactless designs of evaporators have been reported, which could both reduce energy loss and avoid salt scaling.[7,105,106] They provide new avenues to realize high-efficiency solar-driven desalination, and we will discuss these configurations in detail in 4.2.4.

3.2 Increasing the surface area of the evaporator

In addition to introducing a thermal barrier, increasing the evaporation area is another strategy that can promote evaporation efficiency. Firstly, the enlarged evaporation area may also enhance light absorption. Transforming a 2D flat surface into certain 3D morphologies efficiently traps diffuse reflected light and fully utilizes the incident solar light via internal multiple reflections. At the same time, the enlarged surface area provides more evaporation interface for steam escape. For instance, Wang's group developed a 3D origami-based evaporator with the Miura-ori tessellation structure comprised of a periodic concavity pattern.[107] The periodically identical mountain-like and valley-like folds on the evaporator surface enlarged the evaporation area and alleviated light reflection loss (Fig. 5a). Based on a similar origami fold, Li *et al.* fabricated a PPy rose-like evaporator that sustained more reflections by its depth and shape, displaying extraordinary solar absorption above 99%.[108] The dark evaporation rate of the origami rose attained 0.75 kg m^{-2} h^{-1}, 5.4 times of the 2D disk control group (Fig. 5b). In addition, an origami-based switchable 2D/3D evaporator with tunable microstructures and

macroscopic geometries was designed to adapt to the water surface area (Fig. 5f).[109] Wang and co-workers tailored a PPy-coated polyvinylidene fluoride membrane to fit an inversed cone shape for larger surface area.[110] Yu's group constructed a sharply dimpled structure on the surface of a hydrogel-based evaporator to promote evaporation efficiency (Fig. 5d).[111] The constructed nanotextures improved the solar capture capability ascribed to internal multiple reflections and increased the surface area five-fold compared with its shadowed area.

Enhanced evaporation based on the increased area also draws more heat from the surface, leading to a decrease of surface temperature. Following the Stefan-Boltzman equation and Newton's law of cooling, reducing temperature differences between evaporator surface and environment can inhibit heat radiation and convection loss. In this context, a combination of the 1D water path mentioned in 3.1, hollow GO cone,[112] carbonized lotus seedpods,[44] and carbonized sunflower head,[42] which possessed an enlarged evaporation area, were implemented in evaporator design (Fig. 5e g and i). Rational 3D structure designs can maximize the utilization of the solar input and minimize heat radiation and convection loss, which enables the system to approach or even break through the theoretical energy transfer efficiency mentioned above. Wang's group proposed a 3D cylindrical cup-shaped structure where the cup wall was able to recover the diffuse reflectance and heat radiation loss, obtaining a high energy efficiency close to 100% (Fig. 5c).[113] Zhu's group designed a deliberate structure comprised of inner cotton cores (1D water path) and outer plant cellulose wrapping coated with CB nanoparticles (photothermal absorbers), which had high evaporation area.[114] This unique structural design realized superior energy transfer efficiency even over the theoretical limit through gaining energy from the ambient environment, because the temperature of the absorber was constantly below the ambient temperature during the operation (Fig. 5h).

3.3 Recycling of latent heat

The ultimate goal of photothermal evaporation is to obtain freshwater from wastewater or saltwater. Heat is lost during the condensation process for water collection in a conventional process. An effective strategy to promote the overall thermal efficiency, therefore, is recycling the latent heat in an evaporation-condensation cycle, which can be achieved through device and process design. Such approaches enable process efficiencies to significantly exceed 100%. A pioneering study presented by Asinari's group developed an entirely passive multi-stage solar-driven distiller, in which each unit stage stacked vertically was comprised of four layers including an aluminium sheet on the top and a hydrophobic microporous membrane sandwiched between two layers of hydrophilic microfiber (Fig. 6).[115] The hydrophilic layers were connected a protruding strip, and the one immersed in the seawater supplied the feed while the other collected freshwater. A commercial solar absorber was placed on the first aluminium sheet surface for light-to-heat conversion, and a convection reducer and a heat sink were respectively set on the top and bottom of the whole device to further preserve the heat. During the operation process, the heat was conducted through the aluminium sheet from the solar absorber to the seawater within the hydrophilic layer. The vapor passed through the hydrophobic membrane and condensed in the hydrophilic layer at the permeate side. In this design, latent heat was recycled by the next unit stage and ultimately confined by the heat sink on the bottom, enabling continuous desalination with an excellent distillate flow rate of about 3 L m^{-2} h^{-1} under less than one sun irradiation. Salt scaling accumulated in the upper hydrophilic layer could diffuse back to the saline bath by gravity or could be rinsed with extra seawater. A related multi-stage solar-driven membrane distillation device concept was presented by Xue et al., and Wang's group furthered this design by replacing the hydrophobic membrane with an air gap.[116,117]

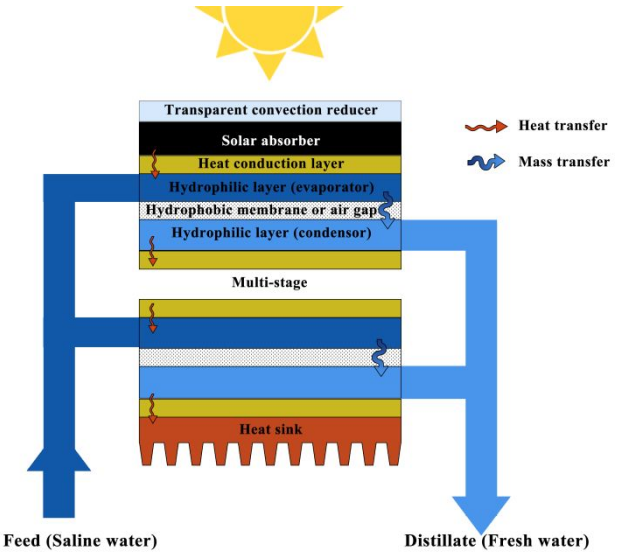

Fig. 6 Multi-stage solar distiller for recycling the latent heat.[115]

In some coupled systems, waste heat during photovoltaic generation can be collected for multi-stage desalination by latent heat recycling, and also the latent heat can be used to generate electricity through a thermoelectric device.[118,119] For example, Li et al. integrated the thermoelectric module with a condensation chamber to recycle the latent heat from steam condensation and generate electriciy.[118] With thermal storage, the electricity generation could be persistent in a prolonged period even without sunlight. The output of electricity depends on the temperature difference between the thermal storage area and the ambient environment. However, despite advanced heat management strategies, latent heat recycling as a side effect of solar distillation inevitablely leads to a relatively low solar-to-electricity efficiency (<1.3%), uneconomic for practical power plants. Wang's group installed a multi-stage membrane distillation device that could recycle the latent heat at the backside of a solar cell.[119] Waste heat from the photovoltaic module was used to drive desalination. Compared with the photothermal-thermoelectric device mentioned above, this combination could generate both electricity and fresh water efficiently.

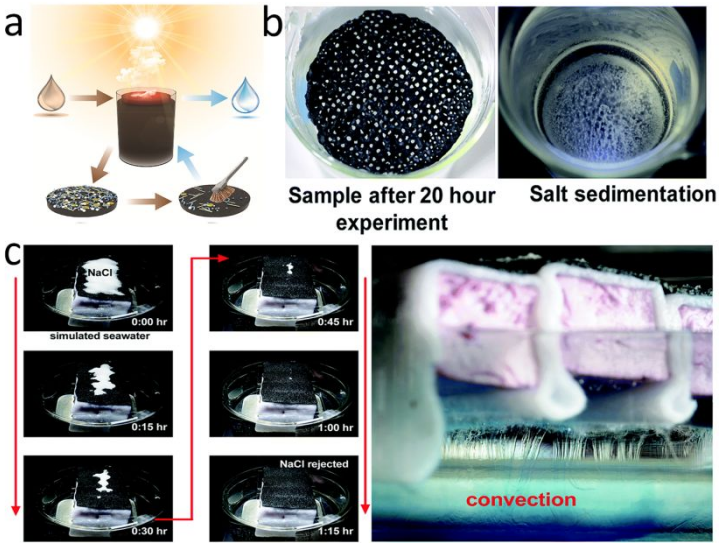

Fig. 7 Wettability designs for anti-scaling. a) A washable and thermostable inorganic solar evaporator;[124] b) anti-scaling performance of a hydrophobic evaporator;[126] c) anti-scaling performance of a superhydrophilic evaporator.[127]

4. How to avoid scaling

Salt scaling is a severe problem for solar-driven evaporators, particularly for desalination applications. In general, the photothermal materials directly contact with the saline water and convert the solar irradiation to heat near the air/water interface to drive evaporation. Rapid evaporation leads to a sharp increase of local ion concentration, and ultimately crystallization at an oversaturated concentration. Scale forms due to the accumulation of salt crystals. Scaling not only blocks the inner channels of porous evaporators thereby hindering water transport, but also covers the surface of the photothermal material and reflects solar irradiation, both of which compromise the evaporation performance and even deteriorate evaporators irreversibly. Avoiding scaling remains a challenge that attracts growing research interest in recent years.

The most straightforward solution is to remove salt precipitation mechanically, such as by hand washing,[120–122] brush scrubbing,[123] or sonication[124]. All of these cleaning processes may damage the photothermal device, imposing additional design constraints on evaporators for durability and/or washability. The mechanical strength of evaporator materials could be enhanced by integrating high-performance photothermal materials (e.g. reduced GO, CNTs, and CB nanoparticles) with inert and flexible natural fabrics (e.g. silk or cotton) or artificial polymer fibers (e.g. nylon 6, polyacrylonitrile, or PS).[120–122,125] Some reported photothermal polymer nanofibers can be hand-washed over 100 times without obvious decline of evaporation efficiency. The bonding strength of the photothermal material/substrate interface could be further enhanced by chemical cross-linking.[123] Beyond polymeric substrates, inorganic materials such as SiC also serve as a robust structural support, which can withstand not only brush scrubbing but also extremely high temperature (1000 °C) for organic contaminant removal (Fig. 7a).[124]

However, mechanical cleaning strategies cannot avoid salt deposition on the evaporators, leading to the interruption of continuous evaporation processes and extra cost. Cleaning treats the symptoms without addressing the root cause of salt scaling. Therefore, wettability and configuration designs have been explored as options to suppress the scaling process.

4.1 Wettability design

One of the effective strategies to reduce scaling is to regulate the wettability of evaporators. Evaporators with hydrophobic modification can prevent saline water infiltration, avoiding scaling in the pores and on the top surface. Moreover, a hydrophobic material is easy to float on the water, localizing the heating at the air/water interface. For example, Kashyap *et al*. fabricated a hydrophobic photothermal film comprised of graphite flakes, carbon fibers, and liquid latex.[126] After hydrophobization, the film could enable long-term evaporation in high-salinity brine without salt clogging (Fig. 7b). However, the light-to-heat interface (LHI) is the top surface while the evaporating interface (EI) is the bottom one in a hydrophobic evaporator. Both the heat transfer from LHI to EI and from EI to the bulk water cause unfavorable heat loss, leading to a relatively low evaporation efficiency (62.7%).

In contrast, superhydrophilic evaporators can deliver outstanding anti-scaling property benefiting from their strong water affinity. These evaporators are normally composed of at least two parts: a hydrophilic photothermal top layer, and a superhydrophilic porous bottom layer. The superhydrophilic

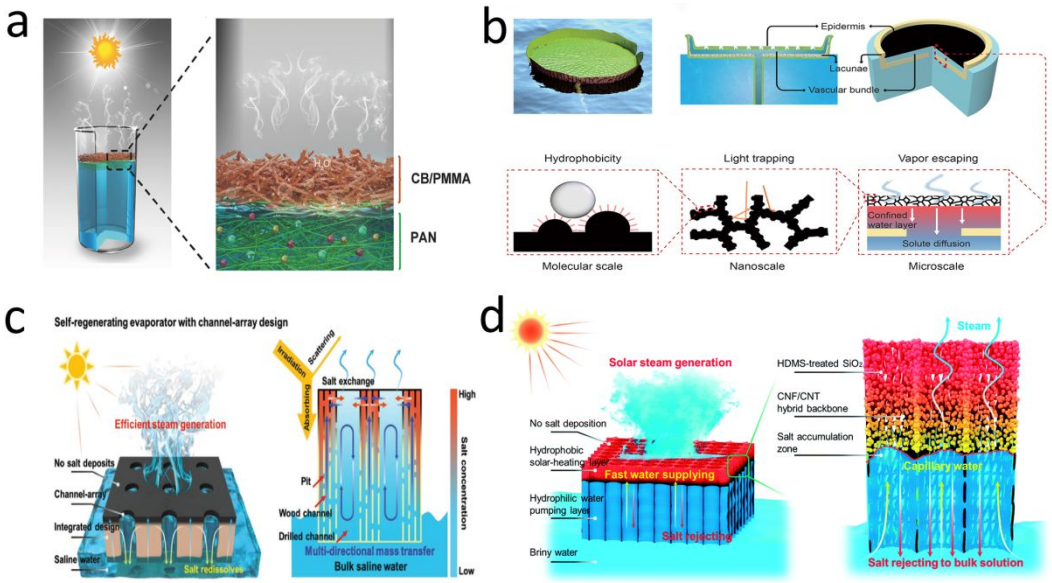

Fig. 8 Structure designs for anti-scaling. a) Self-floating Janus evaporator;[135] b) water-lily-inspired hierarchical design;[136] c) bimodal porous wood with a carbonized surface and its anti-scaling mechanism;[38] d) a Janus evaporator with straight through-pores.[146]

porous substrate supplies sufficient water to dilute the concentrated brine and bring the ions back to the bulk water. Moreover, many systems also include a thick thermo-insulating layer (e.g. PS foam) to reduce the heat loss and float the evaporator on water. For example, Ni and co-workers developed a floating solar evaporator comprising black and white cellulose fabric layers covered on expanded PS foams.[127] The white cellulose fabric was incorporated between the foam layers, providing water channels connecting the top photothermal layer with the bulk water. No obvious performance decline or scaling can be observed after 30 hrs solar illumination, and even the salt deposited artificially on the evaporator would be brought back to the bulk water (Fig. 7c). Similar designs with superhydrophilic water channels were also reported for salt-rejecting evaporators.[128–131]

4.2 Structure design

Scaling on a solar evaporator can be also regulated by architecture design. Scaling-management can be achieved by combining architecture with special wettability, for example, by implementing a Janus configuration. Other configurations, such as straight through-pore configuration, can also realize impressive anti-scaling performance, which will be discussed in the following sections.

4.2.1 Janus configuration

An emerging approach is to take advantage of a Janus configuration with a top hydrophobic photothermal layer and a bottom hydrophilic layer for water wicking. The hydrophobic layer can reject water intrusion and the following scaling, as well as float the evaporators at the air/water interface, while the hydrophilic layer guarantees continuous and adequate water supply to dilute the concentrated solution at the interface.[132–134] Zhu's group constructed a self-floating Janus evaporator integrating two decoupled electrospun nanofibrous layers composed of polymethylmethacrylate and polyacrylonitrile, respectively, followed by spray-deposition of CB nanoparticles.[135] The top layers served as a light absorber while the bottom layer provided a reservoir for water transport (Fig. 8a). The Janus evaporator exhibited stable desalination performance under one sun irradiation. In contrast, a reference hydrophilic material exhibited a 15% decline in evaporation rate after 45 min due to salt scaling. Following this pioneering work, the same group reported a water-lily-inspired hierarchical design consisting of a top hydrophobic absorber and a bottom stand.[136] A thin water layer sandwiched between the top and bottom served for water supply and salt excretion, combining with through-holes of the bottom stand (Fig. 8b). In another example, Yang *et al.* assembled plasmonic gold nanorods onto a single-walled CNT film to fabricate a bilayer Janus membrane for solar steam generation.[137] The upper gold nanorod layer served as the photothermal absorber with the porous network structure for vapor escape, while the bottom single-walled CNT film provided water supply, heat management, and solar absorption enhancement. This Janus membrane exhibited high evaporation efficiency (94%) under five suns irradiation and remained stable for at least 24 cycles. Several groups have also fabricated Janus membrane evaporators by simply filtrating the hydrophobic photothermal materials onto a hydrophilic membrane substrate.[138–140]

Inverse Janus configurations with a hydrophilic top layer and a hydrophobic bottom layer can also be employed in anti-scaling evaporation after incorporating water channels in the hydrophobic layer. Their anti-scaling mechanism is similar to that of hydrophilic evaporators mentioned in section 4.1. For example, Wu *et al.* fabricated an all-carbon nano-architecture comprised of hydrophilic graphene nanopetals and hydrophobic graphene foam.[141] The thick hydrophobic layer not only floated the system, but also acted as a thermo-insulating barrier against heat loss. This material offered stable overall evaporation

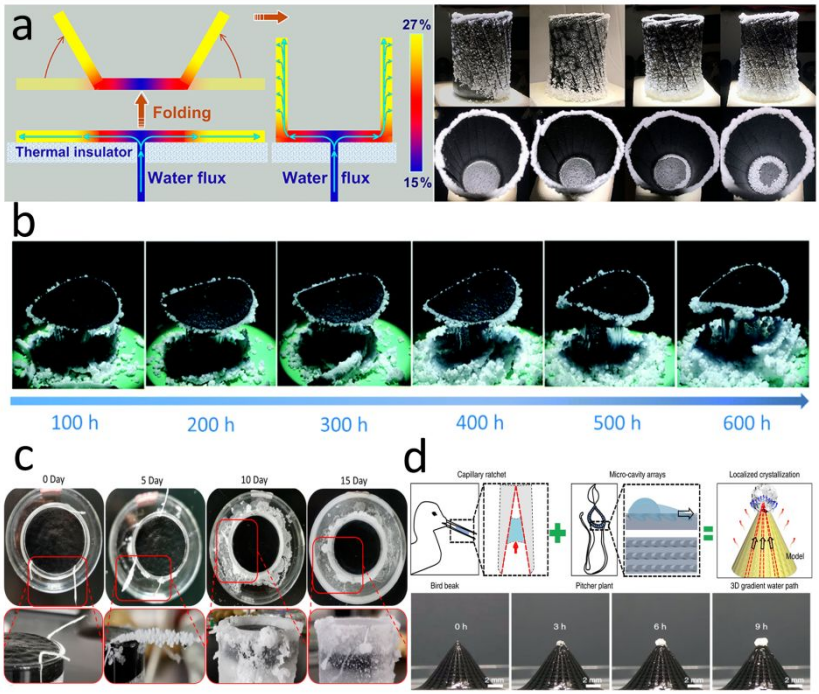

Fig. 9 Salt management in an evaporator. a) Brine transport and salt gradient formed in a photothermal disc with 1D water path;[149] b) salt self-falling evaporator for long-term continuous operation;[150] c) localized salt crystallization phenomenon on a cotton string inserted into an evaporator;[151] d) bird beak and pitcher plant-inspired 3D evaporator for localized crystallization.[152]

efficiency around 88.6% for 240 hours operation without apparent scaling.

4.2.2 Straight through-pore configuration

Inspired by water transport and transpiration of trees, Hu's group proposed a design for efficient solar steam generation based on wood with aligned hydrophilic channels. The wood-based evaporator was fabricated by carbonizing the surface and then applied in seawater desalination and groundwater extraction.[37] The initial vascular wood structure provided plentiful hydrophilic microscopic straight channels, which enabled sufficient water supply for accumulated salt dissolution. Although such design could resist scaling under one sun irradiation, salt accumulation was observed when the evaporation rate increased under five suns irradiation. Following that pioneering work, the same group developed two optimized wood-based evaporators to further promote scaling resistance. Balsa wood with a natural bimodal porous structure was applied to fabricate an anti-scaling evaporator.[39] Such wood includes two sizes of pores, narrow tracheids of 18-39 μm and large vessel channels of 180-390 μm. The micro- and macro-channels are inherently hydrophilic and interconnected with pits, nanopores, and ray parenchyma cells. Benefiting from this distinct microstructure, the saline feed was infiltrated within the channels of balsa wood and delivered to the carbonized surface continuously. Meanwhile, the concentrated brine was diluted by the ion and water diffusion between narrow tracheids and large vessel channels along the concentration gradient. No obvious scaling or performance decline could be observed even under a high evaporation rate (~6.4 kg m^{-2} h^{-1}) and strong irradiation (six suns). In contrast, the evaporation rate of the unimodal reference decreased by ~18% due to visible salt scaling. The American basswood used in their previous work also has bimodal porous structure (narrow tracheids of 5-15 μm, and large vessel of ~50 μm). However, it exhibited poorer scaling resistance compared to the balsa wood because the vessel channels in balsa wood are much larger for water transport from the bulk water to the wood surface and between the narrow tracheids and vessel channels. To further promote the anti-scaling property, Hu's group drilled channels with a diameter around 1 mm to enlarge the vertical pores.[38] Rapid salt ion exchange between microscale natural wood channels and millimeter-sized artificial drilled channels prevented the local concentration increase and crystallization (Fig. 8c). Such evaporators exhibited outstanding long-term stability in solar distillation processes.

Since straight hydrophilic channels can play a prominent role in anti-scaling, such structures have been applied in various anti-scaling evaporator designs. Apart from natural wood, other materials with vertical low-tortuosity channels were also employed in fabricating solar evaporators, such as polyacrylonitrile foam,[142] blank hollow spacer fabric,[143] chitosan/ZnO scaffold,[144] and corn straw-based foam.[145]

Some researchers have also combined both Janus configuration and aligned low-tortuosity channels to achieve a superior scaling resistance. Directional freezing casting is widely used to fabricate supports with aligned straight channels. For example, Hu *et al.* developed a Janus evaporator supported with aligned low-tortuous, hydrophilic channels by freezing casting of cellulose nanofibers, exhibiting more than 80% efficiency (Fig.

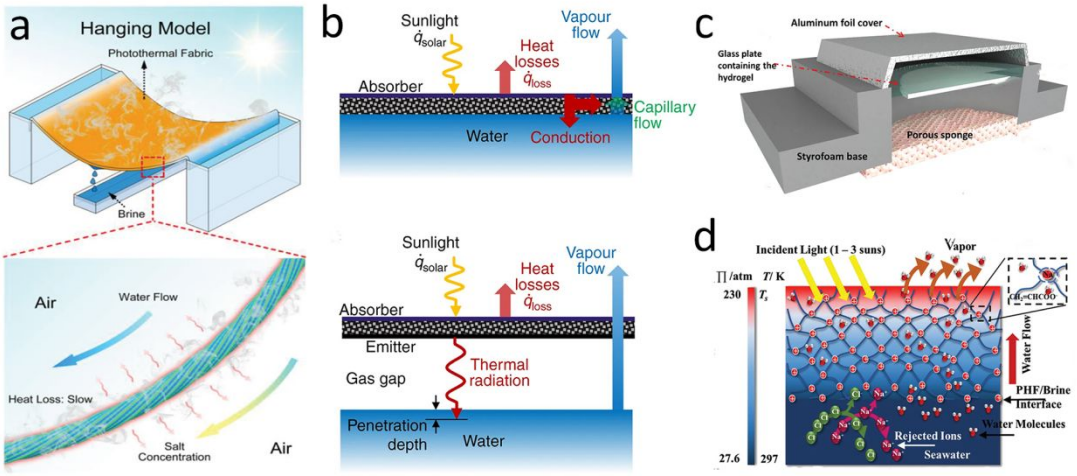

Fig. 10 a) Photothermal hanging model;[105] b) direct-contact and contactless absorbers for thermal irradiation;[106] c) contactless solar-driven evaporator based on a superhygroscopic hydrogel;[153] d) salt-rejection by a highly charged evaporator.[155]

8d).[146] Through a similar directional freeze method, Zhang and co-workers presented a vertically aligned Janus MXene aerogel possessing superior evaporation efficiency (87%) and evaporation rate (about 1.46 kg m^{-2} h^{-1}) under one sun irradiation.[147] The MXene aerogel maintained stable evaporation rate over 15 days without any salt scaling. Similarly, Li *et al.* reported a Janus membrane evaporator with penetrative pore structure fabricated by 2D solvent freezing, which achieved nearly 90.2% evaporation efficiency with a thermal insulator adopted beneath.[148] All of these evaporators exhibited excellent anti-scaling property as well as long-term stability.

4.2.3 Salt-harvesting configuration

Beyond inhibiting scale formation, salt accumulation can alternatively be repurposed by designs intended for salt harvesting. We include these salt-harvesting evaporators in this section because they also require stable, efficient evaporation. Moreover, such evaporators require control over salt precipitation at some designed positions.

In one example, a hydrophilic strip was inserted into the center of a photothermal disc, along which the brine was raised and spread to the edges. A salt concentration gradient formed along the radial direction outward, so that the salt concentration at the far edge reached saturation and led to crystallization, while it remained unsaturated in the central region (Fig. 9a).[149] The only drawback of this configuration is that the salt needs to be removed from the evaporators after a period of time, which cannot be collected continuously. Inspired by the above-mentioned structure, Xia and co-workers developed a similar evaporator composed of a horizontal photothermal disc and a vertical hydrophilic thread inserted into the center of the disc.[150] The binding force between salt and disc was weakened by prewetting the disc with brine, enabling the salt to fall from the disc under gravity (Fig. 9b). Moreover, they further developed a computational fluid dynamics model to make the salt precipitation process predictable and controllable by changing the inlet of feed solution.

In these examples, the hydrophilic thread plays a critical role to guide the water flow. A recent study demonstrated that salt crystallization could be located on a cotton thread inserted into the margin of a superhydrophilic photothermal sponge due to the coffee ring effect (Fig. 9c).[151] Another experiment presented by Wu *et al.* reported a biomimetic 3D structure with controllable salt precipitation.[152] Combining the capillary ratchet of a bird beak and micro-cavity arrays of a pitcher plant, the 3D structure possessed hierarchical pathways to transport the water from the bottom to the apex (Fig. 9d). The cone structure with asymmetric grooves and gradient micro-cavity led to a thickness gradient of water film. During the illumination, the thinner part evaporated faster and brought more heat from the surface, causing a temperature gradient induced surface tension difference according to the Marangoni effect. All of these factors drove and participated the salt dissolved in water to the apex.

4.2.4 Other configurations

An effective way to avoid scaling is to control the ion concentration in the concentrated solution below saturation. Liu *et al.* developed a novel model of evaporation by hanging a hydrophilic photothermal fabric between two brine tanks (Fig. 10a).[105] The brine was wicked through the fabric and gathered at the bottom of the suspended fabric. The fabric exhibited much higher evaporation rate in contrast to fabric floating on the brine because the heating volume of the solution was quite small in the suspended fabric, as well as the heat loss. Concentrated solution dropped from the fabric before saturation.

Quite different from a direct-contact evaporator, a contactless evaporator is separated from the brine, and heats the brine via thermal infrared radiation instead of thermal conduction based on the strong infrared absorption properties of water. In the contactless configuration, the crucial component consists of a selective absorber for solar energy-heat conversion, an emitter for re-emitting thermal radiation, and a gas gap for separating absorber/emitter from brine (Fig. 10b). Cooper et al. first proposed a laboratory-scale contactless evaporator placed in an insulated enclosure and realized superheated steam generation

(133 °C).[106] Additionally, Menon and co-workers introduced a convective cover on the selective absorber to decrease heat loss and fabricated a contactless photothermal umbrella.[7] Absorbing water from the moisture-rich zone above the sea and then desorbing it by solar-driven evaporation is another contactless strategy to avoid salt scaling. Nandakumar *et al.* fabricated a nanoporous superhygroscopic hydrogel with remarkable water-absorption capacity.[153] The hydrogel was separated from seawater by a porous sponge (Fig. 10c). Such a device performed stable water harvesting under absorption/desorption cycles without scaling.

4.3 Surface charge design

Beyond surface wettability and structure, anti-scaling property can be also achieved by regulating the surface charges of the materials based on the Donnan exclusion effect. According to the Donnan effect, water molecules can diffuse through the absorber while cations or anions are rejected due to electrostatic repulsion.

Xiao's group developed a Janus poly(ionic liquid) monolithic solar evaporator, in which the positively charged imidazolium repelled the Na^+ ions.[154] In another study, Zeng *et al.* embedded poly(sodium acrylate) in a microporous carbon foam to fabricate a polyelectrolyte hydrogel evaporator.[155] The water was transported through ionic hydration channels, and the rejection of the ions was ~35%. Although some ions could penetrate through the hydrogel, they were trapped in the hydrogel such that scaling was avoided (Fig. 10d). A thin film composite membrane structure seems particularly effective at rejecting ions.[156]

5. Summary and perspective

In this review, we summarize recent progress on the emerging topic of solar-driven evaporators for water treatment. The key factors affecting evaporation efficiency and long-term performance are discussed. The primary step to construct an ideal evaporator is to select an efficient photothermal material with broad light absorption. Various materials with different light-to-heat mechanisms are included in Section 2. Morphology and arrangement of these materials can also affect the light-to-heat conversion by broadening the absorption spectrum and enabling multiple reflections in the structures. Heat management is essential to promote evaporation efficiency. Introducing a thermal barrier or/and enlarging the evaporation surface area are common approaches to improve heat utilization. For long-term operation in desalination applications, evaporators suffer from severe scaling, which can be alleviated by applying various surface and/or structural designs.

From the view of materials, little room is left to increase light harvesting, because most of the recently reported materials can achieve nearly 100% light absorption. Composite materials are likely to be a focus in future research because they can promote light utilization by broadening the absorption spectrum in the near-infrared region to cover the broad solar irradiation spectrum. Another opportunity lies in the identification of photothermal materials suitable for industrial-scale production, and the carbon materials seem an ideal candidate due to their wide sources, stable properties, low cost, and non-toxicity.

For heat management, significant effort has been devoted to structure design for rapid evaporation and reduced heat loss. Since the temperature difference between the evaporation surface and environment provides the driving force, heat loss can be alleviated by reducing the temperature of the evaporation interface. "Cool evaporation" processes will likely receive more attention in future research, which can be realized by enlarging the evaporation area to bring the heat from the surface rapidly.[113,114,157] Although it may initially seem intuative that a higher surface temperature leads to a higher photothermal efficiency by accelerating evaporation, current research indicates cool evaporation can improve the heat utilization (including the heat from the environment). Furthermore, the latent heat recycling model proposed by Asinari's group holds great promise in practical application because of its efficient heat utilization and easy-to-scale-up design.

For the scaling problem, most current research focuses on promoting water supply to bring the concentrated salt ions back to the bulk. In this strategy, there exists a competition between the water evaporation and ion diffusion from the surface to the bulk, and the faster evaporation requires more water supply to avoid scaling. However, increasing water supply promotes not only mass transfer but also heat transfer, which is detrimental to the heat utilization in evaporation. Therefore, contactless evaporation seems a better choice to address this problem at a fundamental level. Salt rejection devices that exclude the ions before they can reach the evaporating interface are also promising, as described in section 4.3. Importantly, material design, heat management, and scaling control should not be considered independently. For example, surface wettability of photothermal materials will affect both scaling and heat transfer during evaporation.

Evaporation-induced concentration polarization creates a saline gradient from the surface to the bulk, from which energy can be drawn. Yang *et al.* combined solar-driven evaporation with a reverse electrodialysis process to produce both freshwater and clean energy, which inspires future work to utilize the salinity difference.[159] Moreover, the interfacial evaporation-induced temperature gradient[160,161] and water flow[162] can also generate energy by using specific energy collectors. Similarly, the temperature rise and solute (substrate) enrichment could potentially facilitate photocatalytic performance, so a new direction may be to couple solar-driven evaporation with other processes like catalysis to pursue superior performance.

Solar-driven evaporators are poised to transition from a research curiosity to practical desalination and wastewater treatment processes. Opportunities in distributed systems, where traditional large-scale RO plants are not feasible, maybe

particularly appealing. Since direct utilization of solar energy offers sustainability and potential economic advantages, photothermal materials are finding ever-widening applications, such as de-icing,[163] reducing petroleum viscosity for energy-saving transport,[164] and wastewater re-production.[165–168] As more researchers turn their attention to these fascinating systems, one can anticipate even more uses to address a diverse array of social needs.

Conflicts of interest

There are no conflicts to declare.

Acknowledgements

This work was financially supported in part by the National Natural Science Foundation of China (51909291) and the Fundamental Research Funds for the Central Universities (19lgzd17). S.B.D. was supported as part of the Advanced Materials for Energy-Water-Systems (AMEWS) Center, an Energy Frontier Center funded by the U.S. Department of Energy, Office of Science, Basic Energy Sciences.

Notes and references

1 R. G. Taylor, B. Scanlon, P. Döll, M. Rodell, R. Van Beek, Y. Wada, L. Longuevergne, M. Leblanc, J. S. Famiglietti, M. Edmunds, L. Konikow, T. R. Green, J. Chen, M. Taniguchi, M. F. P. Bierkens, A. Macdonald, Y. Fan, R. M. Maxwell, Y. Yechieli, J. J. Gurdak, D. M. Allen, M. Shamsudduha, K. Hiscock, P. J. F. Yeh, I. Holman and H. Treidel, *Nat. Clim. Chang.*, 2013, **3**, 322–329.

2 J. Schewe, J. Heinke, D. Gerten, I. Haddeland, N. W. Arnell, D. B. Clark, R. Dankers, S. Eisner, B. M. Fekete, F. J. Colón-González, S. N. Gosling, H. Kim, X. Liu, Y. Masaki, F. T. Portmann, Y. Satoh, T. Stacke, Q. Tang, Y. Wada, D. Wisser, T. Albrecht, K. Frieler, F. Piontek, L. Warszawski and P. Kabat, *Proc. Natl. Acad. Sci. U. S. A.*, 2014, **111**, 3245–3250.

3 B. Van der Bruggen and C. Vandecasteele, *Desalination*, 2002, **143**, 207–218.

4 L. F. Greenlee, D. F. Lawler, B. D. Freeman, B. Marrot and P. Moulin, *Water Res.*, 2009, **43**, 2317–2348.

5 A. M. Delgado-Torres, L. García-Rodríguez and M. J. del Moral, *Desalination*, 2020, **477**, 114247.

6 C. Catherine, *Desalination*, 2009, **245**, 214–231.

7 A. K. Menon, I. Haechler, S. Kaur, S. Lubner and R. S. Prasher, *Nat. Sustain.*, 2020, **3**, 144–151.

8 O. Neumann, A. S. Urban, J. Day, S. Lal, P. Nordlander and N. J. Halas, *ACS Nano*, 2013, **7**, 42–49.

9 M. S. Zielinski, J. Choi, T. La Grange, M. Modestino, S. Mohammad, H. Hashemi, Y. Pu, S. Birkhold, A. Hubbell and D. Psaltis, *Nano Lett.*, 2016, **16**, 2159–2167.

10 G. Liu, J. Xu and K. Wang, *Nano Energy*, 2017, **41**, 269–284.

11 Z. Deng, J. Zhou, L. Miao, C. Liu, Y. Peng, L. Sun and S. Tanemura, *J. Mater. Chem. A*, 2017, **5**, 7691–7709.

12 M. Gao, L. Zhu, C. K. Peh and G. W. Ho, *Energy Environ. Sci.*, 2019, **12**, 841–864.

13 J. Zhou, Y. Gu, P. Liu, P. Wang, L. Miao, J. Liu, A. Wei, X. Mu, J. Li and J. Zhu, *Adv. Funct. Mater.*, 2019, **29**, 1903255.

14 Y. Zhang, T. Xiong, D. K. Nandakumar and S. C. Tan, *Adv. Sci.*, 2020, **7**, 1903478.

15 F. Zhao, Y. Guo, X. Zhou, W. Shi and G. Yu, *Nat. Rev. Mater.*, 2020, **5**, 388–401.

16 X. Li, G. Ni, T. Cooper, N. Xu, J. Li, L. Zhou, X. Hu, B. Zhu, P. Yao and J. Zhu, *Joule*, 2019, **3**, 1798–1803.

17 C. Chen, Y. Kuang and L. Hu, *Joule*, 2019, **3**, 683–718.

18 P. Wang, *Environ. Sci. Nano*, 2018, **5**, 1078–1089.

19 L. Zhu, M. Gao, C. K. N. Peh and G. W. Ho, *Mater. Horizons*, 2018, **5**, 323–343.

20 H. Ghasemi, G. Ni, A. M. Marconnet, J. Loomis, S. Yerci, N. Miljkovic and G. Chen, *Nat. Commun.*, 2014, **5**, 4449.

21 Y. Liu, J. Chen, D. Guo, M. Cao and L. Jiang, *ACS Appl. Mater. Interfaces*, 2015, **7**, 13645–13652.

22 Y. Wang, L. Zhang and P. Wang, *ACS Sustain. Chem. Eng.*, 2016, **4**, 1223–1230.

23 Z. Yin, H. Wang, M. Jian, Y. Li, K. Xia, M. Zhang, C. Wang, Q. Wang, M. Ma, Q. S. Zheng and Y. Zhang, *ACS Appl. Mater. Interfaces*, 2017, **9**, 28596–28603.

24 J. Lee, P. Srimuk, K. Aristizabal, C. Kim, S. Choudhury, Y. C. Nah, F. Mücklich and V. Presser, *ChemSusChem*, 2017, **10**, 3611–3623.

25 X. Yang, Y. Yang, L. Fu, M. Zou, Z. Li, A. Cao and Q. Yuan, *Adv. Funct. Mater.*, 2018, **28**, 1704505.

26 Y. Fu, G. Wang, T. Mei, J. Li, J. Wang and X. Wang, *ACS Sustain. Chem. Eng.*, 2017, **5**, 4665–4671.

27 X. Hu, W. Xu, L. Zhou, Y. Tan, Y. Wang, S. Zhu and J. Zhu, *Adv. Mater.*, 2017, **29**, 1604031.

28 A. Guo, X. Ming, Y. Fu, G. Wang and X. Wang, *ACS Appl. Mater. Interfaces*, 2017, **9**, 29958–29964.

29 X. Li, W. Xu, M. Tang, L. Zhou, B. Zhu, S. Zhu and J. Zhu, *Proc. Natl. Acad. Sci. U. S. A.*, 2016, **113**, 13953–13958.

30 H. Ren, M. Tang, B. Guan, K. Wang, J. Yang, F. Wang, M. Wang, J. Shan, Z. Chen, D. Wei, H. Peng and Z. Liu, *Adv. Mater.*, 2017, **29**, 1702590.

31 Y. Ito, Y. Tanabe, J. Han, T. Fujita, K. Tanigaki and M. Chen, *Adv. Mater.*, 2015, **27**, 4302–4307.

32 Y. Li, T. Gao, Z. Yang, C. Chen, Y. Kuang, J. Song, C. Jia, E. M. Hitz, B. Yang and L. Hu, *Nano Energy*, 2017, **41**, 201–209.

33 Q. Jiang, L. Tian, K. K. Liu, S. Tadepalli, R. Raliya, P. Biswas, R. R. Naik and S. Singamaneni, *Adv. Mater.*, 2016, **28**, 9400–9407.

34 S. Singh, N. Shauloff and R. Jelinek, *ACS Sustain. Chem. Eng.*, 2019, **7**, 13186–13194.

35 Y. Wang, C. Wang, X. Song, S. K. Megarajan and H. Jiang, *J. Mater. Chem. A*, 2018, **6**, 963–971.
36 H. Yang, Z. Chen, Y. Xie, J. Wang, J. W. Elam, W. Li and S. B. Darling, *Adv. Mater. Interfaces*, 2018, **6**, 1801252.
37 M. Zhu, Y. Li, G. Chen, F. Jiang, Z. Yang, X. Luo, Y. Wang, S. D. Lacey, J. Dai, C. Wang, C. Jia, J. Wan, Y. Yao, A. Gong, B. Yang, Z. Yu, S. Das and L. Hu, *Adv. Mater.*, 2017, **29**, 1704107.
38 Y. Kuang, C. Chen, S. He, E. M. Hitz, Y. Wang, W. Gan, R. Mi and L. Hu, *Adv. Mater.*, 2019, **31**, 1900498.
39 S. He, C. Chen, Y. Kuang, R. Mi, Y. Liu, Y. Pei, W. Kong, W. Gan, H. Xie, E. Hitz, C. Jia, X. Chen, A. Gong, J. Liao, J. Li, Z. J. Ren, B. Yang, S. Das and L. Hu, *Energy Environ. Sci.*, 2019, **12**, 1558–1567.
40 N. Xu, X. Hu, W. Xu, X. Li, L. Zhou, S. Zhu and J. Zhu, *Adv. Mater.*, 2017, **29**, 1606762.
41 J. Li, X. Wang, Z. Lin, N. Xu, X. Li, J. Liang, W. Zhao, R. Lin, B. Zhu, G. Liu, L. Zhou, S. Zhu and J. Zhu, *Joule*, 2020, **4**, 928–937.
42 P. Sun, W. Zhang, I. Zada, Y. Zhang, J. Gu, Q. Liu, H. Su, D. Pantelić, B. Jelenković and D. Zhang, *ACS Appl. Mater. Interfaces*, 2020, **12**, 2171–2179.
43 Y. Bian, Q. Du, K. Tang, Y. Shen, L. Hao, D. Zhou, X. Wang, Z. Xu, H. Zhang, L. Zhao, S. Zhu, J. Ye, H. Lu, Y. Yang, R. Zhang, Y. Zheng and S. Gu, *Adv. Mater. Technol.*, 2019, **4**, 1800593.
44 J. Fang, J. Liu, J. Gu, Q. Liu, W. Zhang, H. Su and D. Zhang, *Chem. Mater.*, 2018, **30**, 6217–6221.
45 L. Zhu, M. Gao, C. K. N. Peh, X. Wang and G. W. Ho, *Adv. Energy Mater.*, 2018, **8**, 1702149.
46 L. Zhou, Y. Tan, D. Ji, B. Zhu, P. Zhang, J. Xu, Q. Gan, Z. Yu and J. Zhu, *Sci. Adv.*, 2016, **2**, e1501227.
47 K. Bae, G. Kang, S. K. Cho, W. Park, K. Kim and W. J. Padilla, *Nat. Commun.*, 2015, **6**, 10103.
48 L. Zhou, S. Zhuang, C. He, Y. Tan, Z. Wang and J. Zhu, *Nano Energy*, 2017, **32**, 195–200.
49 J. Chen, J. Feng, Z. Li, P. Xu, X. Wang, W. Yin, M. Wang, X. Ge and Y. Yin, *Nano Lett.*, 2019, **19**, 400–407.
50 M. Zhu, Y. Li, F. Chen, X. Zhu, J. Dai, Y. Li, Z. Yang, X. Yan, J. Song, Y. Wang, E. Hitz, W. Luo, M. Lu, B. Yang and L. Hu, *Adv. Energy Mater.*, 2018, **8**, 1701028.
51 L. Zhou, Y. Tan, J. Wang, W. Xu, Y. Yuan, W. Cai, S. Zhu and J. Zhu, *Nat. Photonics*, 2016, **10**, 393–398.
52 Y. Lin, Z. Chen, L. Fang, M. Meng, Z. Liu, Y. Di, W. Cai, S. Huang and Z. Gan, *Nanotechnology*, 2018, **30**, 015402.
53 J. Xu, F. Xu, M. Qian, Z. Li, P. Sun, Z. Hong and F. Huang, *Nano Energy*, 2018, **53**, 425–431.
54 D. Wu, D. Qu, W. Jiang, G. Chen, L. An, C. Zhuang and Z. Sun, *J. Mater. Chem. A*, 2019, **7**, 8485–8490.
55 X. Yu, X. Wang, Q. Zhang, J. Li and J. Liu, *J. Appl. Phys.*, 2014, **116**, 073508.
56 L. Zhang, J. Xing, X. Wen, J. Chai, S. Wang and Q. Xiong, *Nanoscale*, 2017, **9**, 12843–12849.
57 J. Liang, H. Liu, J. Yu, L. Zhou and J. Zhu, *Nanophotonics*, 2019, **8**, 771–786.
58 Z. Wang, Y. Liu, P. Tao, Q. Shen, N. Yi, F. Zhang, Q. Liu, C. Song, D. Zhang, W. Shang and T. Deng, *Small*, 2014, **10**, 3234–3239.
59 Y. Liu, S. Yu, R. Feng, A. Bernard, Y. Liu, Y. Zhang, H. Duan, W. Shang, P. Tao, C. Song and T. Deng, *Adv. Mater.*, 2015, **27**, 2768–2774.
60 C. Ma, J. Yan, Y. Huang, C. Wang and G. Yang, *Sci. Adv.*, 2018, **4**, eaas9894.
61 S. Ishii, K. Chen, H. Okuyama and T. Nagao, *Adv. Opt. Mater.*, 2017, **5**, 1600902.
62 G. P. Zograf, M. I. Petrov, D. A. Zuev, P. A. Dmitriev, V. A. Milichko, S. V. Makarov and P. A. Belov, *Nano Lett.*, 2017, **17**, 2945–2952.
63 F. Tao, Y. Zhang, K. Yin, S. Cao, X. Chang, Y. Lei, D. S. Wang, R. Fan, L. Dong, Y. Yin and X. Chen, *ACS Appl. Mater. Interfaces*, 2018, **10**, 35154–35163.
64 C. Zhang, C. Yan, Z. Xue, W. Yu, Y. Xie and T. Wang, *Small*, 2016, 5320–5328.
65 Y. Chang, Z. Wang, Y. E. Shi, X. Ma, L. Ma, Y. Zhang and J. Zhan, *J. Mater. Chem. A*, 2018, **6**, 10939–10946.
66 T. F. Chala, C. M. Wu, M. H. Chou and Z. L. Guo, *ACS Appl. Mater. Interfaces*, 2018, **10**, 28955–28962.
67 G. Zhu, J. Xu, W. Zhao and F. Huang, *ACS Appl. Mater. Interfaces*, 2016, **8**, 31716–31721.
68 M. Ye, J. Jia, Z. Wu, C. Qian, R. Chen, P. G. O'Brien, W. Sun, Y. Dong and G. A. Ozin, *Adv. Energy Mater.*, 2017, **7**, 1601811.
69 J. Wang, Y. Li, L. Deng, N. Wei, Y. Weng, S. Dong, D. Qi, J. Qiu, X. Chen and T. Wu, *Adv. Mater.*, 2017, **29**, 1603730.
70 Y. Zeng, J. Yao, B. A. Horri, K. Wang, Y. Wu, D. Li and H. Wang, *Energy Environ. Sci.*, 2011, **4**, 4074–4078.
71 Q. Zhang, G. Yi, Z. Fu, H. Yu, S. Chen and X. Quan, *ACS Nano*, 2019, **13**, 13196–13207.
72 J. Zhao, Y. Yang, C. Yang, Y. Tian, Y. Han, J. Liu, X. Yin and W. Que, *J. Mater. Chem. A*, 2018, **6**, 16196–16204.
73 R. Li, L. Zhang, L. Shi and P. Wang, *ACS Nano*, 2017, **11**, 3752–3759.
74 M. Kaur, S. Ishii, S. L. Shinde and T. Nagao, *ACS Sustain. Chem. Eng.*, 2017, **5**, 8523–8528.
75 D. Guo and X. Yang, *Sci. China Mater.*, 2019, **62**, 711–718.
76 E. Traver, R. A. Karaballi, Y. E. Monfared, H. Daurie, G. A. Gagnon and M. Dasog, *ACS Appl. Nano Mater.*, 2020, **3**, 2787–2794.
77 L. Yi, S. Ci, S. Luo, P. Shao, Y. Hou and Z. Wen, *Nano Energy*, 2017, **41**, 600–608.
78 L. Zhang, B. Tang, J. Wu, R. Li and P. Wang, *Adv. Mater.*, 2015, **27**, 4889–4894.
79 X. Huang, Y. H. Yu, O. L. De Llergo, S. M. Marquez and Z. Cheng, *RSC Adv.*, 2017, **7**, 9495–9499.
80 F. Zhao, X. Zhou, Y. Shi, X. Qian, M. Alexander, X. Zhao, S. Mendez, R. Yang, L. Qu and G. Yu, *Nat. Nanotechnol.*, 2018, **13**, 489–495.
81 Q. Jiang, H. Gholami Derami, D. Ghim, S. Cao, Y. S. Jun and S. Singamaneni, *J. Mater. Chem. A*, 2017, **5**, 18397–18402.

82 Z. J. Xia, H. C. Yang, Z. Chen, R. Z. Waldman, Y. Zhao, C. Zhang, S. N. Patel and S. B. Darling, *Adv. Mater. Interfaces*, 2019, **6**, 1900254.
83 Z. Wang, M. Han, F. He, S. Peng, S. B. Darling and Y. Li, *Nano Energy*, 2020, **74**, 104886.
84 F. He, M. Han, J. Zhang, Z. Wang, X. Wu, Y. Zhou, L. Jiang, S. Peng and Y. Li, *Nano Energy*, 2020, **71**, 104650.
85 C. Zhang, Z. Chen, Z. Xia, R. Z. Waldman, S. L. Wu, H. C. Yang and S. B. Darling, *Environ. Sci. Water Res. Technol.*, 2020, **6**, 911–915.
86 M. Alberghini, M. Morciano, L. Bergamasco, M. Fasano, L. Lavagna, G. Humbert, E. Sani, M. Pavese, E. Chiavazzo and P. Asinari, *Sci. Rep.*, 2019, **9**, 4701.
87 F. Jiang, H. Liu, Y. Li, Y. Kuang, X. Xu, C. Chen, H. Huang, C. Jia, X. Zhao, E. Hitz, Y. Zhou, R. Yang, L. Cui and L. Hu, *ACS Appl. Mater. Interfaces*, 2018, **10**, 1104–1112.
88 Z. Chen, B. Dang, X. Luo, W. Li, J. Li, H. Yu, S. Liu and S. Li, *ACS Appl. Mater. Interfaces*, 2019, **11**, 26032–26037.
89 W. Zhang, G. Zhang, Q. Ji, H. Liu, R. Liu and J. Qu, *ACS Appl. Mater. Interfaces*, 2019, **11**, 9974–9983.
90 T. Li, H. Liu, X. Zhao, G. Chen, J. Dai, G. Pastel, C. Jia, C. Chen, E. Hitz, D. Siddhartha, R. Yang and L. Hu, *Adv. Funct. Mater.*, 2018, **28**, 1707134.
91 S. Liu, C. Huang, X. Luo and C. Guo, *Appl. Energy*, 2019, **239**, 504–513.
92 K. Yin, S. Yang, J. Wu, Y. Li, D. Chu, J. He and J. A. Duan, *J. Mater. Chem. A*, 2019, **7**, 8361–8367.
93 P. Qiu, F. Liu, C. Xu, H. Chen, F. Jiang, Y. Li and Z. Guo, *J. Mater. Chem. A*, 2019, **7**, 13036–13042.
94 J. Liu, Q. Liu, D. Ma, Y. Yuan, J. Yao, W. Zhang, H. Su, Y. Su, J. Gu and D. Zhang, *J. Mater. Chem. A*, 2019, **7**, 9034–9039.
95 C. Chen, Y. Li, J. Song, Z. Yang, Y. Kuang, E. Hitz, C. Jia, A. Gong, F. Jiang, J. Y. Zhu, B. Yang, J. Xie and L. Hu, *Adv. Mater.*, 2017, **29**, 1701756.
96 L. Shi, Y. Wang, L. Zhang and P. Wang, *J. Mater. Chem. A*, 2017, **5**, 16212–16219.
97 Z. Guo, G. Wang, X. Ming, T. Mei, J. Wang, J. Li, J. Qian and X. Wang, *ACS Appl. Mater. Interfaces*, 2018, **10**, 24583–24589.
98 X. Yin, Y. Zhang, Q. Guo, X. Cai, J. Xiao, Z. Ding and J. Yang, *ACS Appl. Mater. Interfaces*, 2018, **10**, 10998–11007.
99 Y. Zou, X. Chen, W. Guo, X. Liu and Y. Li, *ACS Appl. Energy Mater.*, 2020, **3**, 2634–2642.
100 Y. Luo, B. Fu, Q. Shen, W. Hao, J. Xu, M. Min, Y. Liu, S. An, C. Song, P. Tao, J. Wu, W. Shang and T. Deng, *ACS Appl. Mater. Interfaces*, 2019, **11**, 7584–7590.
101 Q. Gan, T. Zhang, R. Chen, X. Wang and M. Ye, *ACS Sustain. Chem. Eng.*, 2019, **7**, 3925–3932.
102 Y. Li, T. Gao, Z. Yang, C. Chen, W. Luo, J. Song, E. Hitz, C. Jia, Y. Zhou, B. Liu, B. Yang and L. Hu, *Adv. Mater.*, 2017, **29**, 1700981.
103 H. Liu, X. Zhang, Z. Hong, Z. Pu, Q. Yao, J. Shi, G. Yang, B. Mi, B. Yang, X. Liu, H. Jiang and X. Hu, *Nano Energy*, 2017, **42**, 115–121.
104 C. S. Hu, H. J. Li, J. Y. Wang, A. Haleem, X. C. Li, M. Siddiq and W. D. He, *ACS Appl. Energy Mater.*, 2019, **2**, 7554–7563.
105 Z. Liu, B. Wu, B. Zhu, Z. Chen, M. Zhu and X. Liu, *Adv. Funct. Mater.*, 2019, **29**, 1905485.
106 T. A. Cooper, S. H. Zandavi, G. W. Ni, Y. Tsurimaki, Y. Huang, S. V. Boriskina and G. Chen, *Nat. Commun.*, 2018, **9**, 5086.
107 S. Hong, Y. Shi, R. Li, C. Zhang, Y. Jin and P. Wang, *ACS Appl. Mater. Interfaces*, 2018, **10**, 28517–28524.
108 W. Li, Z. Li, K. Bertelsmann and D. E. Fan, *Adv. Mater.*, 2019, **31**, 1900720.
109 F. Ni, P. Xiao, C. Zhang, Y. Liang, J. Gu, L. Zhang and T. Chen, *ACS Appl. Mater. Interfaces*, 2019, **11**, 15498–15506.
110 Y. Wang, C. Wang, X. Song, M. Huang, S. K. Megarajan, S. F. Shaukat and H. Jiang, *J. Mater. Chem. A*, 2018, **6**, 9874–9881.
111 Y. Guo, F. Zhao, X. Zhou, Z. Chen and G. Yu, *Nano Lett.*, 2019, **19**, 2530–2536.
112 X. Li, R. Lin, G. Ni, N. Xu, X. Hu, B. Zhu, G. Lv, J. Li, S. Zhu and J. Zhu, *Natl. Sci. Rev.*, 2018, **5**, 70–77.
113 Y. Shi, R. Li, Y. Jin, S. Zhuo, L. Shi, J. Chang, S. Hong, K. C. Ng and P. Wang, *Joule*, 2018, **2**, 1171–1186.
114 X. Li, J. Li, J. Lu, N. Xu, C. Chen, X. Min, B. Zhu, H. Li, L. Zhou, S. Zhu, T. Zhang and J. Zhu, *Joule*, 2018, **2**, 1331–1338.
115 E. Chiavazzo, M. Morciano, F. Viglino, M. Fasano and P. Asinari, *Nat. Sustain.*, 2018, **1**, 763–772.
116 G. Xue, Q. Chen, S. Lin, J. Duan, P. Yang, K. Liu, J. Li and J. Zhou, *Glob. Challenges*, 2018, **2**, 1800001.
117 Z. Xu, L. Zhang, L. Zhao, B. Li, B. Bhatia, C. Wang, K. L. Wilke, Y. Song, O. Labban, J. H. Lienhard, R. Wang and E. N. Wang, *Energy Environ. Sci.*, 2020, **13**, 830–839.
118 X. Li, X. Min, J. Li, N. Xu, P. Zhu, B. Zhu, S. Zhu and J. Zhu, *Joule*, 2018, **2**, 2477–2484.
119 W. Wang, Y. Shi, C. Zhang, S. Hong, L. Shi, J. Chang, R. Li, Y. Jin, C. Ong, S. Zhuo and P. Wang, *Nat. Commun.*, 2019, **10**, 3012.
120 H. Kou, Z. Liu, B. Zhu, D. K. Macharia, S. Ahmed, B. Wu, M. Zhu, X. Liu and Z. Chen, *Desalination*, 2019, **462**, 29–38.
121 B. Zhu, H. Kou, Z. Liu, Z. Wang, D. K. MacHaria, M. Zhu, B. Wu, X. Liu and Z. Chen, *ACS Appl. Mater. Interfaces*, 2019, **11**, 35005–35014.
122 Y. Jin, J. Chang, Y. Shi, L. Shi, S. Hong and P. Wang, *J. Mater. Chem. A*, 2018, **6**, 7942–7949.
123 C. Finnerty, L. Zhang, D. L. Sedlak, K. L. Nelson and B. Mi, *Environ. Sci. Technol.*, 2017, **51**, 11701–11709.
124 L. Shi, Y. Shi, R. Li, J. Chang, N. Zaouri, E. Ahmed, Y. Jin, C. Zhang, S. Zhuo and P. Wang, *ACS Sustain. Chem. Eng.*, 2018, **6**, 8192–8200.
125 Q. Zhang, X. Xiao, G. Wang, X. Ming, X. Liu, H. Wang, H. Yang, W. Xu and X. Wang, *J. Mater. Chem. A*, 2018, **6**, 17212–17219.

126 V. Kashyap, A. Al-Bayati, S. M. Sajadi, P. Irajizad, S. H. Wang and H. Ghasemi, *J. Mater. Chem. A*, 2017, **5**, 15227–15234.
127 G. Ni, S. H. Zandavi, S. M. Javid, S. V. Boriskina, T. A. Cooper and G. Chen, *Energy Environ. Sci.*, 2018, **11**, 1510–1519.
128 C. Liu, C. Cai and X. Zhao, *ACS Sustain. Chem. Eng.*, 2020, **8**, 1548–1554.
129 Y. Liu, Z. Liu, Q. Huang, X. Liang, X. Zhou, H. Fu, Q. Wu, J. Zhang and W. Xie, *J. Mater. Chem. A*, 2019, **7**, 2581–2588.
130 Q. Fang, T. Li, H. Lin, R. Jiang and F. Liu, *ACS Appl. Energy Mater.*, 2019, **2**, 4354–4361.
131 Y. Xu, D. Liu, H. Xiang, S. Ren, Z. Zhu, D. Liu, H. Xu, F. Cui and W. Wang, *J. Memb. Sci.*, 2019, **586**, 222–230.
132 H. C. Yang, J. Hou, V. Chen and Z. K. Xu, *Angew. Chemie - Int. Ed.*, 2016, **55**, 13398–13407.
133 R. Z. Waldman, H. C. Yang, D. J. Mandia, P. F. Nealey, J. W. Elam and S. B. Darling, *Adv. Mater. Interfaces*, 2018, **5**, 1800658.
134 H. C. Yang, Y. Xie, J. Hou, A. K. Cheetham, V. Chen and S. B. Darling, *Adv. Mater.*, 2018, **30**, 1801495.
135 W. Xu, X. Hu, S. Zhuang, Y. Wang, X. Li, L. Zhou, S. Zhu and J. Zhu, *Adv. Energy Mater.*, 2018, **8**, 1702884.
136 N. Xu, J. Li, Y. Wang, C. Fang, X. Li, Y. Wang, L. Zhou, B. Zhu, Z. Wu, S. Zhu and J. Zhu, *Sci. Adv.*, 2019, **5**, eaaw7013.
137 Y. Yang, X. Yang, L. Fu, M. Zou, A. Cao, Y. P. Du, Q. Yuan and C. H. Yan, *ACS Energy Lett.*, 2018, **3**, 1165-1171.
138 Y. Yang, H. Zhao, Z. Yin, J. Zhao, X. Yin, N. Li, D. Yin, Y. Li, B. Lei, Y. Du and W. Que, *Mater. Horizons*, 2018, **5**, 1143–1150.
139 Y. Yang, W. Que, J. Zhao, Y. Han, M. Ju and X. Yin, *Chem. Eng. J.*, 2019, **373**, 955–962.
140 D. Qin, Y. Zhu, R. Yang and Z. Xiong, *Nanoscale*, 2020, **12**, 6717-6728
141 S. Wu, G. Xiong, H. Yang, B. Gong, Y. Tian, C. Xu, Y. Wang, T. Fisher, J. Yan, K. Cen, T. Luo, X. Tu, Z. Bo and K. (Ken) Ostrikov, *Adv. Energy Mater.*, 2019, **9**, 1901286.
142 Q. Zhang, H. Yang, X. Xiao, H. Wang, L. Yan, Z. Shi, Y. Chen, W. Xu and X. Wang, *J. Mater. Chem. A*, 2019, **7**, 14620–14628.
143 F. Wang, D. Wei, Y. Li, T. Chen, P. Mu, H. Sun, Z. Zhu, W. Liang and A. Li, *J. Mater. Chem. A*, 2019, **7**, 18311–18317.
144 X. Y. Wang, J. Xue, C. Ma, T. He, H. Qian, B. Wang, J. Liu and Y. Lu, *J. Mater. Chem. A*, 2019, **7**, 16696–16703.
145 J. Li, X. Zhou, P. Mu, F. Wang, H. Sun, Z. Zhu, J. Zhang, W. Li and A. Li, *ACS Appl. Mater. Interfaces*, 2020, **12**, 798–806.
146 R. Hu, J. Zhang, Y. Kuang, K. Wang, X. Cai, Z. Fang, W. Huang, G. Chen and Z. Wang, *J. Mater. Chem. A*, 2019, **7**, 15333–15340.
147 Q. Zhang, G. Yi, Z. Fu, H. Yu, S. Chen and X. Quan, *ACS Nano*, 2019, **13**, 13196–13207.
148 H.-H. Yu, L.-J. Yan, Y.-C. Shen, S.-Y. Chen, H.-N. Li, J. Yang and Z.-K. Xu, *Research*, 2020, **2020**, 1–11.
149 Y. Shi, C. Zhang, R. Li, S. Zhuo, Y. Jin, L. Shi, S. Hong, J. Chang, C. Ong and P. Wang, *Environ. Sci. Technol.*, 2018, **52**, 11822–11830.
150 Y. Xia, Q. Hou, H. Jubaer, Y. Li, Y. Kang, S. Yuan, H. Liu, M. W. Woo, L. Zhang, L. Gao, H. Wang and X. Zhang, *Energy Environ. Sci.*, 2019, **12**, 1840–1847.
151 J. Li, X. Zhou, J. Zhang, C. Liu, F. Wang, Y. Zhao, H. Sun, Z. Zhu, W. Liang and A. Li, *ACS Appl. Energy Mater.*, 2020, **3**, 3024-3032.
152 L. Wu, Z. Dong, Z. Cai, T. Ganapathy, N. X. Fang, C. Li, C. Yu, Y. Zhang and Y. Song, *Nat. Commun.*, 2020, **11**, 521.
153 D. K. Nandakumar, Y. Zhang, S. K. Ravi, N. Guo, C. Zhang and S. C. Tan, *Adv. Mater.*, 2019, **31**, 1806730.
154 C. Xiao, W. Liang, L. Chen, J. He, F. Liu, H. Sun, Z. Zhu and A. Li, *ACS Appl. Energy Mater.*, 2019, **2**, 8862–8870.
155 J. Zeng, Q. Wang, Y. Shi, P. Liu and R. Chen, *Adv. Energy Mater.*, 2019, **9**, 1900552.
156 X. Ma, W. Fang, W. Ying, D. Chen, Z. Li, Z. Deng, C. Gao and X. Peng, *Appl. Mater. Today*, 2020, **18**, 100459.
157 H. Song, Y. Liu, Z. Liu, M. H. Singer, C. Li, A. R. Cheney, D. Ji, L. Zhou, N. Zhang, X. Zeng, Z. Bei, Z. Yu, S. Jiang and Q. Gan, *Adv. Sci.*, 2018, **5**, 1800222.
158 Y. Zhang, T. Xiong, D. K. Nandakumar and S. C. Tan, *Adv. Sci.*, 2020, **7**, 1903478.
159 P. Yang, K. Liu, Q. Chen, J. Li, J. Duan, G. Xue, Z. Xu, W. Xie and J. Zhou, *Energy Environ. Sci.*, 2017, **10**, 1923–1927.
160 Q. Shen, Z. Ning, B. Fu, S. Ma, Z. Wang, L. Shu, L. Zhang, X. Wang, J. Xu, P. Tao, C. Song, J. Wu, T. Deng and W. Shang, *J. Mater. Chem. A*, 2019, **7**, 6514–6521.
161 L. Zhu, T. Ding, M. Gao, C. K. N. Peh and G. W. Ho, *Adv. Energy Mater.*, 2019, **9**, 1900250.
162 T. Ding, K. Liu, J. Li, G. Xue, Q. Chen, L. Huang, B. Hu and J. Zhou, *Adv. Funct. Mater.*, 2017, **27**, 1700551.
163 S. Wu, Y. Du, Y. Alsaid, D. Wu, M. Hua, Y. Yan, B. Yao, Y. Ma, X. Zhu and X. He, *Proc. Natl. Acad. Sci. U. S. A.*, 2020, 202001972.
164 S. Lyu, Y. He, Y. Yao, M. Zhang and Y. Wang, *Adv. Funct. Mater.*, 2019, **29**, 1900703.
165 H. Geng, Q. Xu, M. Wu, H. Ma, P. Zhang, T. Gao, L. Qu, T. Ma and C. Li, *Nat. Commun.*, 2019, **10**, 1512.
166 Q. Fang, G. Li, H. Lin and F. Liu, *J. Mater. Chem. A*, 2019, **7**, 8960–8966.
167 Z. Sun, J. Wang, Q. Wu, Z. Wang, Z. Wang, J. Sun and C. J. Liu, *Adv. Funct. Mater.*, 2019, **29**, 1901312.
168 W. Huang, P. Su, Y. Cao, C. Li, D. Chen, X. Tian, Y. Su, B. Qiao, J. Tu and X. Wang, *Nano Energy*, 2020, **69**, 104465.